Materials Chemistry and Physics 255 (2020) 123558

Contents lists available at ScienceDirect

Materials Chemistry and Physics

journal homepage: www.elsevier.com/locate/matchemphys

Suppression of σ-phase in nanocrystalline CoCrFeMnNiV high entropy alloy by unsolicited contamination during mechanical alloying and spark plasma sintering

M. Vaidya [a,b,*], Anirudha Karati [c], K. Guruvidyathri [a,d], M. Nagini [a], K.G. Pradeep [a,e], B.S. Murty [a]

[a] Department of Metallurgical & Materials Engineering, Indian Institute of Technology Madras, Chennai, 600036, India
[b] Department of Materials Science and Metallurgical Engineering, Indian Institute of Technology Hyderabad, Kandi, Sangareddy, 502285, Telangana, India
[c] Department of Chemistry, Indian Institute of Technology Madras, Chennai, 600036, India
[d] School of Engineering Sciences and Technology, University of Hyderabad, Gachibowli, Hyderabad, 500046, India
[e] Materials Chemistry, RWTH Aachen University, Kopernikusstr.10, 52074, Aachen, Germany

HIGHLIGHTS

- Cast CoCrFeMnNiV shows 71 vol% of sigma (σ) phase enriched in Cr and V.
- σ-phase is avoided in nanocrystalline CoCrFeMnNiV formed by MA-SPS route.
- Un-solicited contamination of during MA-SPS leads to suppression of σ phase.
- Calphad based *G* vs composition plots are used to explain absence of σ phase.

GRAPHICAL ABSTRACT

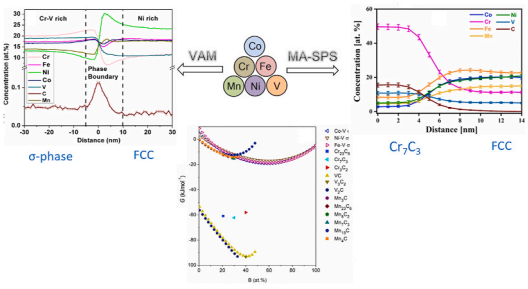

ARTICLE INFO

Keywords:
High-entropy alloy
Nanocrystalline materials
Spark plasma sintering
Atom probe tomography
Calphad

ABSTRACT

CoCrFeMnNiV high entropy alloy (HEA) exhibits a high content of σ-phase (70 vol%) when produced by casting route. In the present work, a combination of mechanical alloying (MA) and spark plasma sintering (SPS) has been used to synthesize nanocrystalline CoCrFeMnNiV HEA where the formation of σ-phase has been avoided. Electron microscopy and atom probe tomography analysis indicated the formation of FCC structured HEA matrix along with (Cr,V) carbide (15 vol%) precipitation, without the presence of σ-phase in SPS processed alloy. Gibbs energy vs composition (*G*-*x*) diagrams of binary subsystems and possible carbides and oxides substantiate the absence of σ-phase during SPS of CoCrFeMnNiV alloy. Thus, the unsolicited contamination during MA-SPS route proves beneficial in suppressing the complex phase formation.

1. Introduction

High entropy alloys (HEAs) represent a new class of multicomponent alloys, which have generated fundamental inquisitiveness and shown encouraging technological potential. Although initial research in HEAs was driven towards identifying single phase HEAs, it has now been

* Corresponding author. Department of Metallurgical & Materials Engineering, Indian Institute of Technology Madras, Chennai, 600036, India.
E-mail address: vaidyam@msme.iith.ac.in (M. Vaidya).

https://doi.org/10.1016/j.matchemphys.2020.123558
Received 23 May 2020; Received in revised form 10 July 2020; Accepted 13 July 2020
Available online 18 July 2020

realised that true single phase HEAs are either scarce or those compositions exhibiting single phases are stabilized in their metastable states which upon equilibrium treatment decompose into multi-phase alloy [1–3]. The maximized configurational entropy (ΔS_{mix}) of HEAs does not guarantee the formation of single phase solid solutions in many of the investigated alloys [4]. Rather, formation of multiple phases is widely reported in HEAs. For example, sigma (σ) phase, which is frequently observed in binary phase diagrams of Ni or Fe based alloys while involving Cr/V as one of the constituents, and accordingly, the formation of σ-phase is widely reported in Cr/V containing HEAs [5,6]. CoCrFeNi and CoCrFeMnNi HEAs, for example, show a thermally stable single-phase FCC structure when processed through casting [7].

Addition of V to CoCrFeMnNi HEA leads to the formation of σ-phase when synthesized by casting route [6]. CoCrFeMnNiV system, even though has high ΔS_{mix} of 1.79 R, displays nearly 70 vol% of σ-phase [5,6], consequently poor ductility and therefore remains largely unexplored. While small quantities of intermetallic phases have been shown to be advantageous [8], presence of complex structures in large fraction embrittles HEA leading to poor ductility [5]. V being a refractory element, retaining it in single phase FCC might have potential improvement in structural properties, particularly at high temperatures. Mechanical alloying (MA) is a widely used approach to produce nanocrystalline materials and the non-equilibrium nature of the process leads to extended solid solubility of alloying elements [9]. MA has also been increasingly used to synthesize nanocrystalline HEAs with formation of simple solid solution structures [10]. Additionally, nanocrystalline HEAs have shown improved strength [11] and promising functional properties [12]. Spark plasma sintering (SPS) has become an increasingly attractive option for the consolidation of MAed powders [13], owing to the shorter processing times relative to conventional sintering and thus ensuring better retention of nanocrystallinity.

In the present work, we aim to study the phase evolution in CoCrFeMnNiV HEA by processing it through MA followed by SPS. To make a detailed comparison with equilibrium structures, CoCrFeMnNiV HEA has also been synthesized by vacuum arc melting. Usage of binary Gibbs energy vs composition (*G-x*) plots, calculated using Calphad models, has been reported to be successful in understanding phase formation and stability in HEAs [14,15]. In the present study, such plots have been utilized for understanding phase formation in CoCrFeMnNiV HEA. The inevitable carbon and oxygen pick-up during milling are duly considered in the thermodynamic analysis to provide novel insights into the phase formation during MA-SPS. In order to predict the relative stability of competing phases, Ellingham diagram can be utilized. However, it can be used only to know the competition among similar phases, e.g. between oxides or between carbides. More importantly, phase diagram calculation requires Calphad database inclusive of all the constituent elements along with C and O, which are not prevalent. In such a scenario, to understand the competition among different types of phases, such as oxides, carbides and solid solution and intermetallic phases that generally form in transition metal systems, *G-x* plots are utilized. To the best of our knowledge, CoCrFeMnNiV HEA has not yet been produced in nanocrystalline state or through any non-equilibrium processing routes.

2. Methods

2.1. Alloy preparation and characterization

Solid pieces (99.5 wt% purity) of Co, Cr, Fe, Mn, Ni and V, in equiatomic proportions, were melt in an arc melting furnace to form bulk CoCrFeMnNiV HEA. The melting chamber was first evacuated to 10^{-5} mbar pressure, and subsequently the melting was carried out in a highly purified Ar atmosphere. Each alloy was re-melted 4–5 times to improve the chemical homogeneity. The buttons were sealed in quartz tube under Ar atmosphere and homogenized at 1473 K for 50 h. Elemental powders of Co, Cr, Fe, Mn, Ni and V (99.5% pure) were milled together in a high energy planetary ball mill (Fritsch Pulverisette P-5) at 300 rpm with a ball to powder weight ratio of 10:1 to obtain nanocrystalline CoCrFeMnNiV HEA. Toluene was used as process controlling agent in milling media of tungsten carbide (WC) vials and balls. The milled powders were consolidated by SPS in Dr. Sinter unit (Model SPS-625, SPS Syntex Inc., Japan) at a temperature of 1173 K for 5 min at a pressure of 60 MPa. X-ray diffraction (XRD) analysis, using Panalytical X-ray diffractometer with Cu-Kα radiation, was used for phase identification.

Nanocrystalline microstructure and phase analysis of the sintered sample was determined using transmission electron microscopy (TEM) in a FEI-Tecnai-T20, 200 kV microscope. Atom probe tomography (APT) measurements were performed on homogenized alloy, using a CAMECA local electrode atom probe (LEAP™) 4000X HR, with the tips prepared using a FEI Helios Nanolab 660 dual beam microscope. APT measurements of the alloy processed through SPS were performed using LEAP 5000 XR. Both the measurements were performed in laser pulsing mode using 355 nm wavelength (UV) laser beam while APT tip was maintained at a temperature of 60 K. The pulse frequency of 200 kHz, laser energy of 25 pJ and a detection rate of 0.5% per evaporation pulse were utilized for both the samples. The needle shaped APT specimens of the SPS sample were prepared using a dual beam workstation, Helios G4 UX focused ion beam/scanning electron microscope (FIB/SEM). Hardness measurements were performed on the bulk and sintered samples using a load of 500 gf with a dwell time of 10s on a Wolpert Wilson Vickers Hardness instrument. Reported values are an average of 10 readings across the pellet.

2.2. Computation of G-x plots

G-x plots were generated for the stable phases of all the binary subsystems in CoCrFeMnNiV alloy at 1273 K. *G-x* data was also calculated for stable binary carbides of the elements in HEA. In these cases, FCC was chosen as the reference state for ease of comparison. In order to find stable phases for the *G-x* plots, binary phase diagrams were first calculated. Thermo-Calc software with TCHEA2 database was used for these calculations. For calculating the *G-x* data for oxides, SSUB5 database was used, since TCHEA2 does not include O. The reference state in this set of calculations was the standard elemental reference. For the sake of comparison *G-x* data for the carbides of V were also calculated using SSUB5.

3. Results and discussion

3.1. Phase formation in bulk CoCrFeMnNiV HEA

Fig. 1a displays the XRD pattern of cast and homogenized CoCrFeMnNiV HEA, where peaks corresponding to tetragonal (σ) (major phase) and FCC phases can be observed. Using quantitative XRD analysis, the volume fraction of σ-phase is estimated to be 70%, which is in close agreement with the previous reports [5,6] on bulk CoCrFeMnNiV. To determine the localised composition of σ and FCC phases accurately, APT measurements have been performed. The APT tips were site-specifically lifted-out from a grain boundary region decorated by the second phase (Fig. 1b). Ni enrichment was observed in the elemental distribution map and it was delineated using a 18 at.% iso-concentration surface shown in Fig. 1c. Corresponding proximity histogram shown in Fig. 1d indicates Cr and V enrichment and, concomitant Ni and Mn enrichment, on either side of the grain boundary indicating the potential σ phase formation. The compositions of the FCC and σ-phases have been presented in Table 1, which further substantiate the excess Cr and V (18.42 and 17.84 at.%, respectively) in the σ-phase.

3.2. Phase evolution in CoCrFeMnNiV during MA-SPS

Phase evolution during MA of CoCrFeMnNiV is depicted in Fig. 2a. The major phase is FCC from initial hours of milling. BCC phase is also

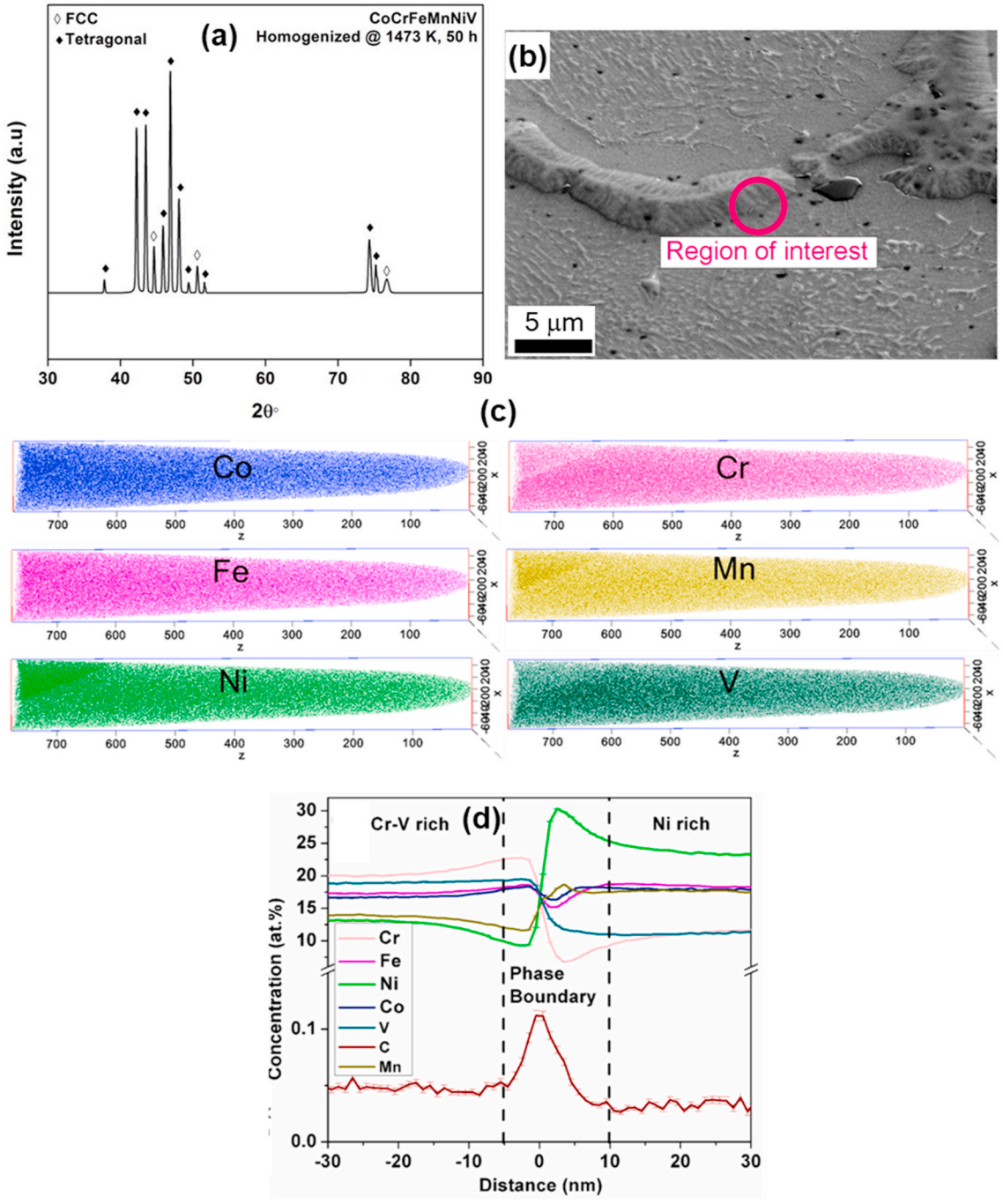

Fig. 1. a) XRD pattern of as cast and homogenized CoCrFeMnNiV HEA, b) SEM SE image of the alloy showing the near grain-boundary phase, c) Ni iso-concentration surface in this region along with the elemental maps and d) the corresponding concentration profiles.

Table 1
Composition (at.%) of major phases in CoCrFeMnNiV HEA after casting and homogenization and MA-SPS.

Element	C	O	Co	Cr	Fe	Mn	Ni	V
After homogenization (Determined using APT)								
Tetragonal	–	–	16.2 ± 0.3	18.2 ± 0.4	17.5 ± 0.2	14.7 ± 0.3	14.8 ± 0.1	18.6 ± 0.2
FCC	–	–	16.8 ± 0.1	12.7 ± 0.2	15.6 ± 0.3	17.9 ± 0.4	23.0 ± 0.1	13.9 ± 0.3
After SPS (Determined using TEM-EDS)								
FCC	–	–	21.1 ± 0.3	13.6 ± 0.5	20.5 ± 0.3	17.8 ± 0.3	22.0 ± 1.0	5.0 ± 0.5
Cr_7C_3	46.2 ± 3.1	–	4.3 ± 0.6	24.9 ± 0.4	5.4 ± 0.2	5.8 ± 0.8	3.5 ± 1.1	9.6 ± 0.6
V–O	10.2 ± 2.2	24.4 ± 1.2	6.5 ± 0.7	9.0 ± 1.1	6.7 ± 0.8	6.9 ± 0.6	6.6 ± 0.7	35.6 ± 0.9
Cr–C–O	22.2 ± 2.6	26.0 ± 2.2	2.8 ± 0.8	27.4 ± 3.5	4.5 ± 1.2	4.7 ± 1.2	3.5 ± 0.8	8.7 ± 0.5

observed, which dissolves into Ni-based FCC matrix after 12 h. Elemental peaks of Mn and Co are observed until 8 h of milling, while WC contamination appears after 10 h of milling. The final alloy, after 15 h, consists of a major FCC phase along with minor fractions of WC. Broadening of XRD peaks with milling time indicates the formation of nanocrystalline grains within the powders and the presence of lattice strain. Formation of FCC phase proceeds via dissolution of Co and Fe in Ni-lattice, which have high mutual solubility as reflected in their binary phase diagrams [16]. Further, the lattice parameter (determined using single peak (111) method) of initial FCC phase (after 3 h of MA) is close to that of Ni (0.352 nm), which slightly increases to 0.359 nm after 15 h of MA. The XRD patterns of sintered alloy, milled powders and as-homogenized alloy are compared in Fig. 2b. After SPS, the alloy consists of the matrix FCC phase along with WC that is retained from milled condition and additional Cr_7C_3 phase. Cr, among all constituents, has highest tendency to form carbides [17] as is apparent in the present study. From quantitative XRD analysis, the volume fraction of Cr_7C_3 is estimated to be approximately 15%. This is in close agreement to the carbide fraction reported for other Cr containing HEAs like CoCrFeNi and CoCrFeMnNi formed by MA-SPS [18,19].

Fig. 2c shows TEM bright field image of sintered CoCrFeMnNiV HEA confirming the presence of nanocrystalline grains. A higher magnification image (Fig. 2d) shows the distribution of different phases within the nanocrystalline grains. The composition of different phases has been determined using EDS (Table 1), which shows that the FCC phase is depleted in Cr and V. The Cr and V depletion arises due to the formation of their respective carbides and oxides. Two kinds of oxide particles are seen, one which is rich in Cr (indexed as Cr–O) and other which is rich in V (indexed as V–O). Presence of Cr–O could arise due to the oxidation of some Cr_7C_3 particles. Selected area diffraction (SAD) patterns depicted in Fig. 2e and f substantiate the orthorhombic and FCC structure of Cr_7C_3 and the matrix phase, respectively. The grain size distribution of FCC phase (Fig. 2g) reveals the average grain size value to be 86 ± 10 nm. It may be noted that no evidence for σ-phase formation could be found during the TEM investigations on a large number of thin foils of consolidated sample.

To obtain the composition of the nano-scale phases in the alloy after SPS in greater detail, APT investigations have been carried out and the results are presented in Fig. 3. The 3–D reconstruction of a typical CoCrFeMnNiV measurement is shown in Fig. 3 including individual ion maps (Fig. 3a) of the constituent elements. Significant Cr enrichment is observed and has been demarcated using a 20 at.% Cr iso-concentration

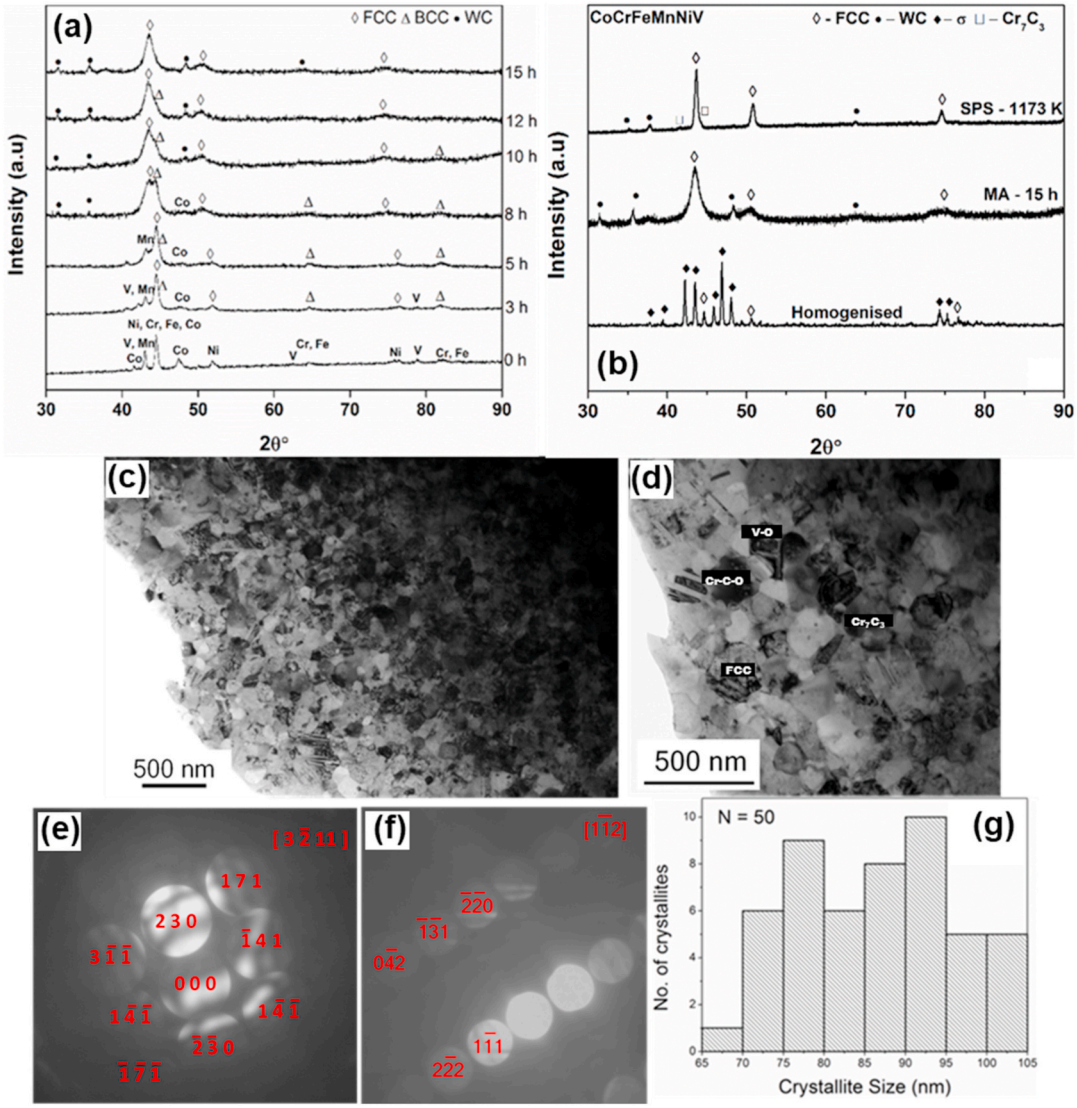

Fig. 2. XRD patterns showing a) phase evolution in CoCrFeMnNiV during MA, b) structure of the alloy subjected to homogenization, MA and SPS, c) low and d) high magnification bright field images of CoCrFeMnNiV HEA processed through SPS. SAD patterns of e) orthorhombic Cr_7C_3, f) FCC matrix and g) Grain size distribution for FCC phase.

surface (Fig. 3b). The one-dimensional concentration profile in Fig. 3c generated from the 10 nm diameter cylindrical region of interest shown in Fig. 3b confirms the presence of Cr carbide, which is in agreement with the results from XRD and TEM. In addition, traces of oxides of V (VO and VO_2) have also been observed as shown in Fig. 3a Formation of VC has also been observed from the 3–D elemental maps of Co, Cr, Fe, Mn, Ni and V presented in Fig. 4a. Proximity histogram corresponding to the 7.3 at. % C iso−concentration interfaces (Fig. 4b) have been plotted as shown in Fig. 4c. The presence of VC is clearly reflected as the concentration of C and V increased rapidly and that of Co, Cr, Fe, Mn and Ni reduced drastically.

The contamination during MA is often inevitable. The oxygen pick-up can occur from the atmosphere or during handling of nanocrystalline powders. The mechanism of C incorporation has still not been identified with certainty. Vaidya et al. [19] have recently shown that Cr_7C_3 formation begins during milling stage itself, and gets enhanced during thermal exposure for e.g. during consolidation by SPS. The carbon containing compounds present during milling are WC (vials and balls) and toluene. However, WC being a stable carbide is unlikely to dissociate and therefore most probable source of C contamination is argued to be decomposition of toluene [19,20]. Although the carbon pick-up during MA of HEAs is unsolicited and some efforts have been directed to reduce the carbide contents (see for e.g. Ref. [21]), a limited fraction of carbide has shown some beneficial effects as well. AlCoCrFe HEA has demonstrated excellent phase stability and very high hardness due to the presence of Cr rich $M_{23}C_6$ carbides [22]. Cr_7C_3 particles present in CoCrFeNi and CoCrFeMnNi alloys after SPS pin the grain boundaries to restrict the grain growth in these HEAs [23].

3.3. G-x plot of the competing phases in CoCrFeMnNiV

It is clear from above sections that the σ-phase present in homogenized CoCrFeMnNiV is absent in the alloy processed through MA and SPS. Although Cr_7C_3 is observed after SPS, its volume fraction (~15%) is significantly less than the amount of σ-phase (~70%) present in cast alloy. To understand the suppression of σ-phase during the adopted MA-SPS route, *G-x* diagrams have been utilized.

Fig. 5a shows *G-x* plots for the stable phases in binary subsystems of CoCrFeMnNiV at 1273 K. It is evident that *G* of V containing σ-phases (Co–V, Ni–V, Fe–V) is highly negative, followed by Cr, which forms σ-phase with Co and Mn. With this dominance in the *G* competition, σ-phase dominates the material produced via casting route. Also, there are no known kinetic constraints on the nucleation of this complex phase, as high thermal energy is available during solidification. Though

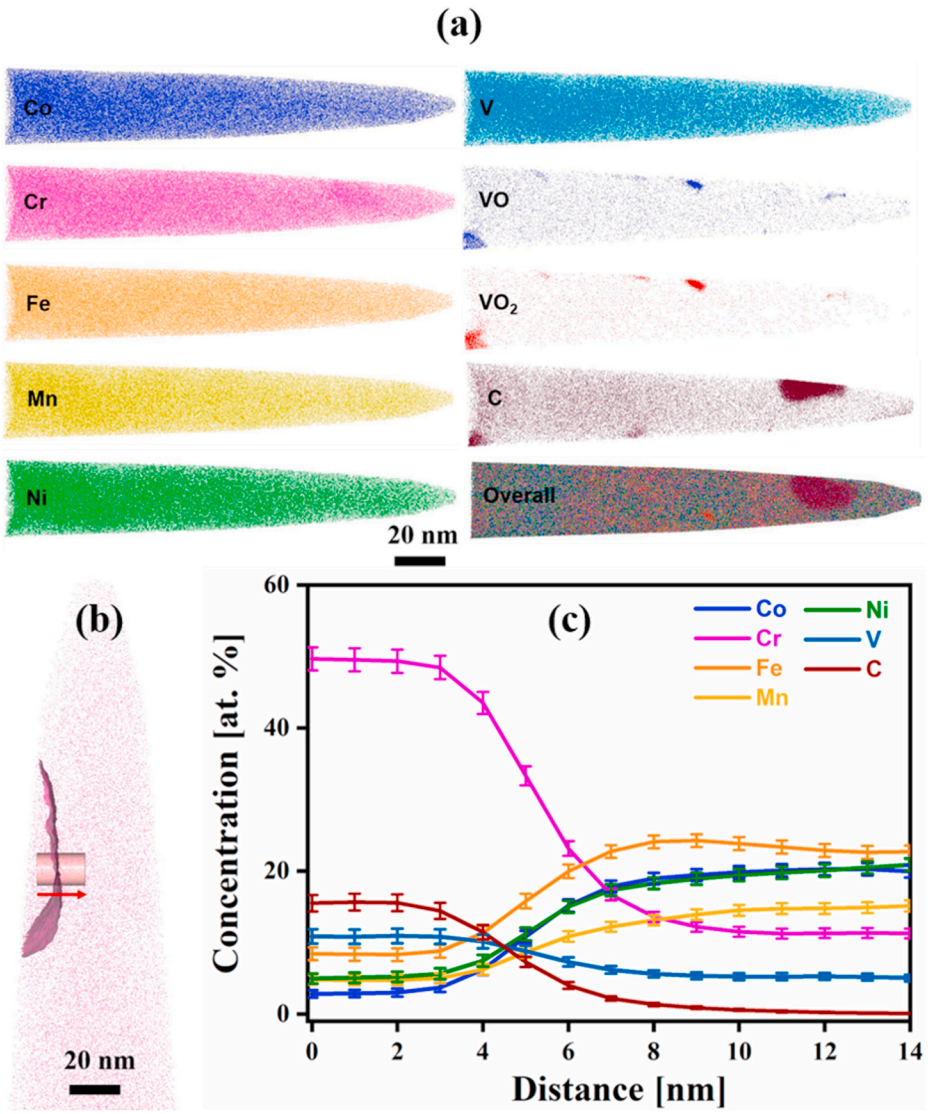

Fig. 3. (a) Elemental distribution of Co, Cr, Fe, Mn, Ni and V with Cr rich carbides, (b) 20 at.% Cr iso–concentration surface and (c) elemental concentration profiles generated from the 10 nm diameter cylindrical region of interest shown in (b).

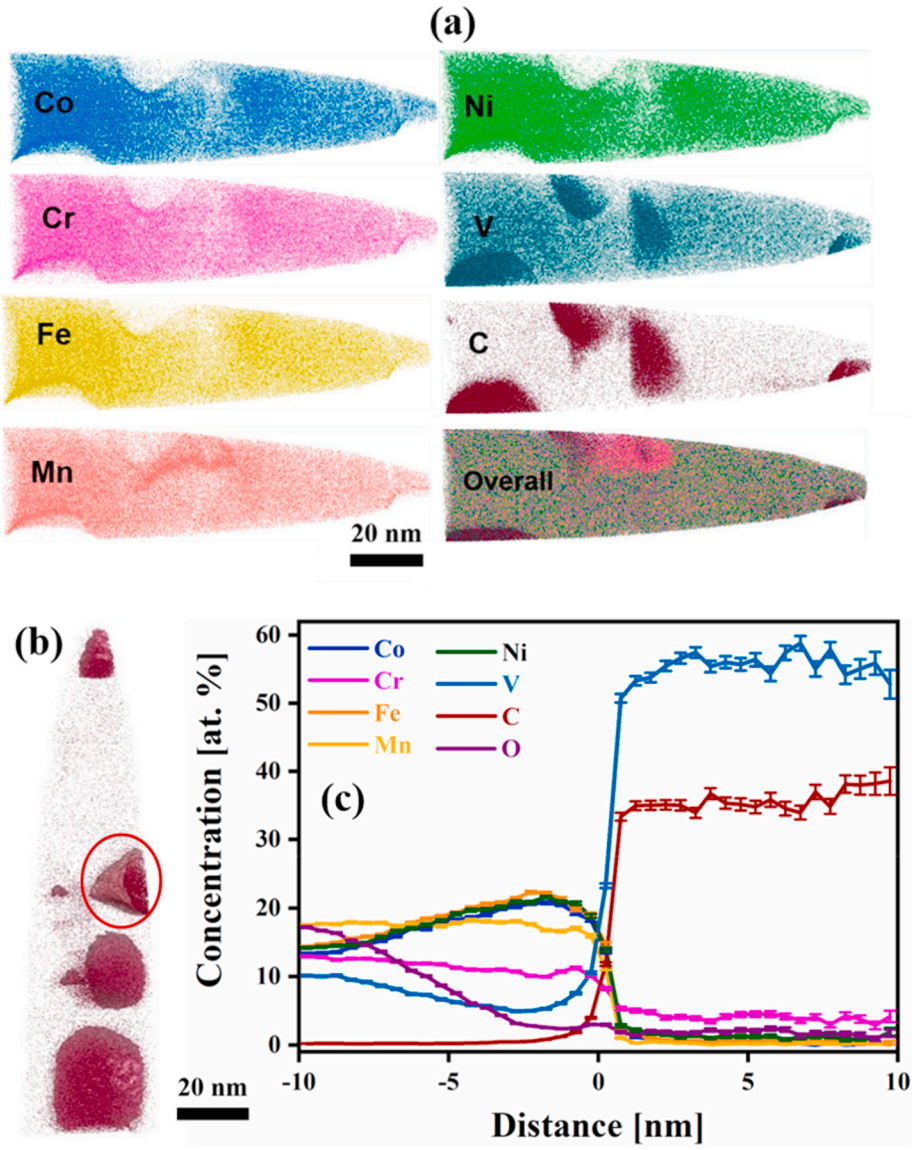

Fig. 4. (a) Elemental distribution of Co, Cr, Fe, Mn, Ni and V with carbides delineated using 7.3 at.% C iso–concentration surface (b) and (c) representative proximity histogram corresponding to the carbide (encircled in (b)) with 0.5 nm bin width.

Cr–V BCC phase also has one of the lowest of *G* values, it does not become stable in HEA. The reason being both these elements are σ-phase formers with the other elements in the HEA. Therefore, the HEA is expected to have a major σ-phase in microstructure, which is observed in the casting route.

When the alloy is formed using SPS (preceded by MA), one may expect to obtain a more equilibrium microstructure due to thermal exposure. However, we have conclusively shown that no σ-phase is present even after SPS. This can be explained by comparing *G-x* diagrams of carbides and possible σ-phases. In Fig. 5b, the *G-x* plots of dominant σ-phases from Fig. 5a are taken and compared with the stable binary carbides. Carbides of V and Cr are highly stable than other carbides and σ-phases. Therefore, due to the higher driving force, the carbide phases form preferentially. Once the carbides have formed, the remaining alloy gets depleted in Cr and V, and therefore do not reach the desired composition to nucleate any σ-phase. Fig. 5b also suggests that the carbides of V are the most stable followed by carbides of Cr. In experiments, however, the carbide is found to have more Cr rather than V (Fig. 2).

The reason can be understood from Fig. 5c. It shows comparison between the *G-x* data of carbides of V and stable oxides of all the elements in HEA. V has the highest tendency of oxide formation as reflected in its multiple oxides (VO, V_2O_3, V_2O_4 and V_2O_5) having highly negative Gibbs energy, followed by Cr. Therefore, the experimentally observed oxide phase is dominated in V content. Since, more V gets into this oxide, the experimentally observed carbide phase is not dominated V, but the next strong carbide former namely, Cr. The preferential oxidation of V during MA and its adverse effect on σ-phase stability has also been exemplified for binary alloys such as $Fe_{48.1}V_{51.9}$ [24–26].

It may be noted that the *G-x* diagram compares the minima in *G* values for various binary phases. However, the phase stability competition in binary subsystems cannot be considered directly to represent the HEA behaviour and the inferences may carry uncertainties in the multicomponent space.

3.4. Absence of σ-phase after MA-SPS of CoCrFeMnNiV – a kinetic perspective

The thermodynamic analysis present above explains that a higher driving force is present for the formation of carbides and oxides than

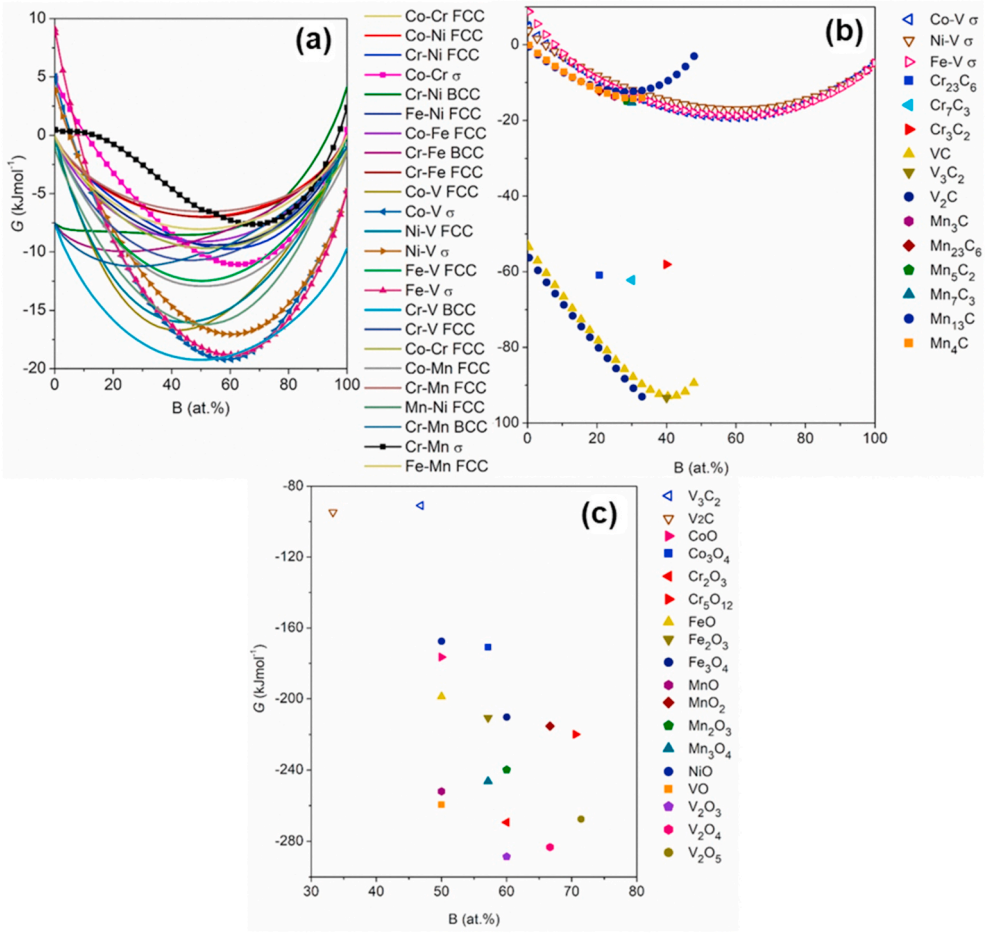

Fig. 5. *G-x* plots at 1273 K for a) binary subsystems (A–B) in Co–Cr–Fe–Mn–Ni–V HEA system, b) dominant binary σ-phases from a) and possible binary carbides with the HEA system, and c) dominant binary carbides from b) and possible binary oxides with the HEA system. B in carbides and oxides is C and O, respectively.

that for σ-phase. MA being a non-equilibrium process, it is also important to briefly discuss the kinetic factors affecting the precipitation of σ-phase. The evolution of σ-phase during non-equilibrium processing routes has been investigated previously for binary [27–29] and ternary alloys [30]. MA, in general, provides both favourable scenario as well as kinetic constraints for the precipitation of σ-phase. MA is a solid state process and takes place at room temperature, hence complex phases are difficult to nucleate [9]. However, the σ-phase formation can be promoted by increased fraction of GBs in some cases. For instance, Costa et al. [30] showed that the formation of σ-phase in Fe–Cr equiatomic alloy formed by MA is enhanced due to a higher fraction of grain boundaries (GBs).

However, when Sn is added (2–6 at.%) to Fe–Cr alloy, Sn precipitates at the GBs and blocks the nucleating sites for σ-phase, thereby suppressing its formation. The reduction in σ-phase content due to Sn precipitation at GBs has been observed for cast alloys as well [32]. The ratio of Fe/Cr is not altered significantly by Sn addition in small amount, hence the composition still remains favourable for σ-phase formation, although its content is reduced. During MA of CoCrFeMnNiV HEA, all the constituents of CoCrFeMnNiV alloy belong to 3d transition series in the periodic table and hence do not differ significantly in their atomic sizes. This facilitates the formation of FCC and BCC structures during MA (Fig. 2a). The nanocrystallinity of powders leads to reduced diffusion distances and aids in achieving enhanced solid solubility [9]. The precipitation of Cr–V carbides, on thermal exposure during SPS, leads to the depletion of Cr and V in the matrix, and their content is no longer sufficient to form σ-phase in the alloy. Therefore, even though the GB fraction is increased after SPS of CoCrFeMnNiV alloy, we do not see any σ-phase formation as evinced by APT and TEM.

The role of contaminants during MA-SPS of HEAs has also been exemplified in literature (although the thermodynamic explanations using G-x plots have never been discussed). The quinary CoFeMnNiV alloy is reported to have σ-phase after MA and SPS, in which C or O contamination is avoided [33,34]. Praveen et al. [22] have demonstrated that the unsolicited C addition during MA-SPS provides excellent phase stability and very high hardness to AlCoCrFe due to the formation of $M_{23}C_6$ carbides. Grain growth kinetics have shown to be restricted in CoCrFeNi and CoCrFeMnNi HEAs after SPS, due to the GB pinning by Cr_7C_3 particles [23].

3.5. Hardness of as-homogenized CoCrFeMnNiV alloy after SPS

It is important to briefly highlight the significance of suppressing σ-phase formation for the mechanical behaviour of CoCrFeMnNiV HEA. The bulk CoCrFeMnNiV reported through casting route shows σ-phase fraction of ~70%. The Vickers hardness measurements for this alloy reveal a hardness of 770 ± 26 HV. Salishchev et al. [5] reported similar hardness values and 0 ductility for this alloy with similar microstructure. They assessed, assuming rule of mixture to be applicable, hardness of σ-phase (H_σ) to be 1002 HV. For the SPS CoCrFeMnNiV HEA used in the present work, the hardness value was 525 ± 35 HV. The alloy after SPS has three contributions to hardness, namely solid solution strengthening from multi-element HEA matrix, grain refinement due to nanocrystalline microstructure and precipitation strengthening arising from second-phase particles of carbides and oxides. Recently John et al. [21] estimated the hardness of Cr_7C_3 phase (H_{Cr7C3}) to be 85 HV formed

during MA-SPS of $Al_{0.3}$CoCrFeNi HEA. Clearly, $H_\sigma \gg H_{Cr7C3}$, therefore embrittlement caused by σ phase is much higher than carbide particles. In fact, it has been shown that CoCrFeMnNi and CoCrFeNi HEAs processed by MA-SPS route exhibit reasonable ductility [18,35] along with high strength, which is derived from second phase particles.

4. Conclusions

The present results demonstrate the phase evolution in CoCrFeMnNiV HEA during MA-SPS and the role of unsolicited contaminations in suppressing σ-phase formation. Microstructure of cast and homogenized CoCrFeMnNiV exhibited the presence of 70 vol% brittle, tetragonal σ-phase, while no σ-phase was observed after MA and on consolidation by SPS. Although, the alloy processed through SPS exhibits majority FCC phase presence, the identification of Cr_7C_3 and minor fractions of oxide particles substantiates impurity phase formation. *G-x* diagrams have been used to demonstrate that when C and O are present, appearance of Cr and V containing carbides/oxides is more favourable than σ-phase formation in CoCrFeMnNiV HEA. The preferential formation of carbides/oxides leads to the depletion of Cr and V content in the alloy, which is insufficient to nucleate σ-phase. Nanocrystallinity of powders is retained after the SPS and average crystallite size of ~86 nm is obtained. This ensures that the elimination of σ-phase does not drastically decrease the hardness of the alloy processed through SPS, grain-refinement and precipitation strengthening contribute to high strength of the CoCrFeMnNiV.

Declaration of competing interest

The authors declare that they have no known competing financial interests or personal relationships that could have appeared to influence the work reported in this paper.

CRediT authorship contribution statement

M. Vaidya: Conceptualization, Investigation, Validation, Writing - original draft, Writing - review & editing. **Anirudha Karati:** Investigation, Writing - review & editing. **K. Guruvidyathri:** Investigation, Writing - review & editing. **M. Nagini:** Investigation, Writing - review & editing. **K.G. Pradeep:** Investigation, Writing - review & editing. **B.S. Murty:** Conceptualization, Supervision, Writing - review & editing.

Acknowledgements

The authors gratefully acknowledge National Facility for Atom Probe Tomography (NFAPT) for carrying out APT studies.

References

[1] F. Otto, A. Dlouhý, K.G. Pradeep, M. Kuběnová, D. Raabe, G. Eggeler, E.P. George, Decomposition of the single-phase high-entropy alloy CrMnFeCoNi after prolonged anneals at intermediate temperatures, Acta Mater. 112 (2016) 40–52, https://doi.org/10.1016/j.actamat.2016.04.005.
[2] Z. Li, K.G. Pradeep, Y. Deng, D. Raabe, C.C. Tasan, Metastable high-entropy dual-phase alloys overcome the strength–ductility trade-off, Nature 534 (2016) 227–230, https://doi.org/10.1038/nature17981.
[3] K.G. Pradeep, C.C. Tasan, M.J. Yao, Y. Deng, H. Springer, D. Raabe, Non-equiatomic high entropy alloys: approach towards rapid alloy screening and property-oriented design, Mater. Sci. Eng. A 648 (2015) 183–192, https://doi.org/10.1016/j.msea.2015.09.010.
[4] Z. Liu, Y. Lei, C. Gray, G. Wang, Examination of solid-solution phase formation rules for high entropy alloys from atomistic Monte Carlo simulations, JOM (J. Occup. Med.) 67 (2015) 2364–2374, https://doi.org/10.1007/s11837-015-1508-3.
[5] G.A. Salishchev, M.A. Tikhonovsky, D.G. Shaysultanov, N.D. Stepanov, A. V. Kuznetsov, I.V. Kolodiy, A.S. Tortika, O.N. Senkov, Effect of Mn and v on structure and mechanical properties of high-entropy alloys based on CoCrFeNi system, J. Alloys Compd. 591 (2014) 11–24, https://doi.org/10.1016/j.jallcom.2013.12.210.
[6] N.D. Stepanov, D.G. Shaysultanov, G.A. Salishchev, M.A. Tikhonovsky, E. E. Oleynik, A.S. Tortika, O.N. Senkov, Effect of v content on microstructure and mechanical properties of the CoCrFeMnNiVx high entropy alloys, J. Alloys Compd. 628 (2015) 170–185, https://doi.org/10.1016/j.jallcom.2014.12.157.
[7] M. Vaidya, K. Guruvidyathri, B.S. Murty, Phase formation and thermal stability of CoCrFeNi and CoCrFeMnNi equiatomic high entropy alloys, J. Alloys Compd. 774 (2019) 856–864, https://doi.org/10.1016/j.jallcom.2018.09.342.
[8] J.Y. He, H. Wang, H.L. Huang, X.D. Xu, M.W. Chen, Y. Wu, X.J. Liu, T.G. Nieh, K. An, Z.P. Lu, A precipitation-hardened high-entropy alloy with outstanding tensile properties, Acta Mater. 102 (2016) 187–196, https://doi.org/10.1016/j.actamat.2015.08.076.
[9] B.S. Murty, S. Ranganathan, Novel materials synthesis by mechanical alloying/milling, Int. Mater. Rev. 43 (1998) 101–141, https://doi.org/10.1179/imr.1998.43.3.101.
[10] M. Vaidya, G.M. Muralikrishna, B.S. Murty, High-entropy alloys by mechanical alloying: a review, J. Mater. Res. 34 (2019) 664–686, https://doi.org/10.1557/jmr.2019.37.
[11] B. Schuh, F. Mendez-Martin, B. Völker, E.P. George, H. Clemens, R. Pippan, A. Hohenwarter, Mechanical properties, microstructure and thermal stability of a nanocrystalline CoCrFeMnNi high-entropy alloy after severe plastic deformation, Acta Mater. 96 (2015) 258–268, https://doi.org/10.1016/j.actamat.2015.06.025.
[12] Y. Zhang, T. Zuo, Y. Cheng, P.K. Liaw, High-entropy alloys with high saturation magnetization, electrical resistivity, and malleability, Sci. Rep. 3 (2013) 1–7, https://doi.org/10.1038/srep01455.
[13] M. Omori, Sintering, consolidation, reaction and crystal growth by the spark plasma system (SPS), Mater. Sci. Eng. A. 287 (2000) 183–188, https://doi.org/10.1016/S0921-5093(00)00773-5.
[14] K. Guruvidyathri, K.C. Hari Kumar, J.W. Yeh, B.S. Murty, Topologically close-packed phase formation in high entropy alloys: a review of Calphad and experimental results, JOM (J. Occup. Med.) 69 (2017) 2113–2124, https://doi.org/10.1007/s11837-017-2566-5.
[15] K. Guruvidyathri, B.S. Murty, J.W. Yeh, K.C.H. Kumar, Gibbs energy-composition plots as a tool for high-entropy alloy design, J. Alloys Compd. 768 (2018) 358–367, https://doi.org/10.1016/j.jallcom.2018.07.264.
[16] ASM Handbook, Alloy phase diagrams, ASM Int. 3 (1992) 1741.
[17] S.R. Shatynski, The thermochemistry of transition metal carbides, Oxid. Met. 13 (1979) 105–118, https://doi.org/10.1007/BF00611975.
[18] S. Praveen, J. Basu, S. Kashyap, R.S. Kottada, Exceptional resistance to grain growth in nanocrystalline CoCrFeNi high entropy alloy at high homologous temperatures, J. Alloys Compd. 662 (2016) 361–367, https://doi.org/10.1016/j.jallcom.2015.12.020.
[19] M. Vaidya, A. Karati, A. Marshal, K.G. Pradeep, B.S. Murty, Phase evolution and stability of nanocrystalline CoCrFeNi and CoCrFeMnNi high entropy alloys, J. Alloys Compd. 770 (2019) 1004–1015, https://doi.org/10.1016/J.JALLCOM.2018.08.200.
[20] K. Vasanthakumar, N.S. Karthiselva, N.M. Chawake, S.R. Bakshi, Formation of TiCx during reactive spark plasma sintering of mechanically milled Ti/carbon nanotube mixtures, J. Alloys Compd. 709 (2017) 829–841, https://doi.org/10.1016/j.jallcom.2017.03.216.
[21] R. John, A. Karati, M.M. Garlapati, M. Vaidya, R. Bhattacharya, D. Fabijanic, B. S. Murty, Influence of mechanically activated annealing on phase evolution in Al0.3CoCrFeNi high-entropy alloy, J. Mater. Sci. 54 (2019) 14588–14598, https://doi.org/10.1007/s10853-019-03917-7.
[22] S. Praveen, A. Anupam, R. Tilak, R.S. Kottada, Phase evolution and thermal stability of AlCoCrFe high entropy alloy with carbon as unsolicited addition from milling media, Mater. Chem. Phys. 210 (2018) 57–61, https://doi.org/10.1016/j.matchemphys.2017.10.040.
[23] M. Vaidya, A. Anupam, J.V. Bharadwaj, C. Srivastava, B.S. Murty, Grain growth kinetics in CoCrFeNi and CoCrFeMnNi high entropy alloys processed by spark plasma sintering, J. Alloys Compd. 791 (2019) 1114–1121, https://doi.org/10.1016/J.JALLCOM.2019.03.341.
[24] B.F.O. Costa, G. Le Caër, B. Malaman, The effect of oxygen on ball milling of a near-equiatomic FeV sigma phase, J. Appl. Phys. 104 (2008), https://doi.org/10.1063/1.3005876, 084315.
[25] B.F.O. Costa, G. Le Caër, B. Malaman, Evolution of a FeV sigma phase ball-milled in a mixture of argon and air, Hyperfine Interact. 183 (2008) 67–73, https://doi.org/10.1007/s10751-008-9760-3.
[26] B.F.O. Costa, G. Le Caër, B. Malaman, A.C. Batista, Mössbauer spectroscopy and X-ray diffraction studies of ball-milling-induced transformations of a near-equiatomic FeV sigma phase: influence of oxygen, Nucl. Instrum. Methods Phys. Res., Sect. A 580 (2007) 404–407, https://doi.org/10.1016/j.nima.2007.05.065.
[27] B.F.O. Costa, J. Cieslak, S.M. Dubiel, Kinetics of σ-phase formation in equiatomic cold-rolled Fe-V alloys, Mater. Chem. Phys. 143 (2013) 19–25, https://doi.org/10.1016/j.matchemphys.2013.07.020.
[28] J. Cieślak, B.F.O. Costa, S.M. Dubiel, G. Le Caër, Kinetics of the sigma-to-alpha phase transformation caused by ball milling in near equiatomic Fe-Cr alloys, Phys. Rev. B 73 (2006) 184123, https://doi.org/10.1103/PhysRevB.73.184123.
[29] S.M.D.B.F. O Costa, J. Cieślak, Study of a sigma-phase formation in an equiatomic Fe-V alloy, J. Phys. Conf. Ser. 217 (2010), 012077, https://iopscience.iop.org/article/10.1088/1742-6596/217/1/012077/meta. (Accessed 9 July 2020).
[30] B.F.O. Costa, G. Le Caër, N.A. de Campos, Study of alpha–sigma phase transformation in mechanically alloyed Fe–Cr–Sn alloys, Phys. Status Solidi 183 (2001) 235–250, https://doi.org/10.1002/1521-396X(200102)183:2<235::AID-PSSA235>3.0.CO;2-Z.
[32] B.F.O. Costa, G. Le Caër, N. Ayres de Campos, On the role of tin solubility in the precipitation of the sigma-phase in Fe–Cr–Sn alloys, Phys. Stat. Sol. 164 (1997) 687, https://doi.org/10.1002/1521-396X(199712)164:2<687::AID-PSSA687>3.0.CO;2-S.

[33] F. Alijani, M. Reihanian, K. Gheisari, Study on phase formation in magnetic FeCoNiMnV high entropy alloy produced by mechanical alloying, J. Alloys Compd. 773 (2019) 623–630, https://doi.org/10.1016/j.jallcom.2018.09.204.
[34] F. Alijani, M. Reihanian, K. Gheisari, M. Yuasa, H. Miyamoto, Microstructural characterization of mechanically alloyed FeCoNiMnV high entropy alloy consolidated by spark plasma sintering, Adv. Eng. Mater. (2019), https://doi.org/10.1002/adem.201901311.
[35] H. Hadraba, Z. Chlup, A. Dlouhy, F. Dobes, P. Roupcova, M. Vilemova, J. Matejicek, Oxide dispersion strengthened CoCrFeNiMn high-entropy alloy, Mater. Sci. Eng. A. 689 (2017) 252–256, https://doi.org/10.1016/j.msea.2017.02.068.